JACS
JOURNAL OF THE AMERICAN CHEMICAL SOCIETY

Article

pubs.acs.org/JACS

Colloidal Monolayer β-In_2Se_3 Nanosheets with High Photoresponsivity

Guilherme Almeida,[†,#] Sedat Dogan,[†] Giovanni Bertoni,[†,⊥] Cinzia Giannini,[∥] Roberto Gaspari,[†,§] Stefano Perissinotto,[‡] Roman Krahne,[†] Sandeep Ghosh,[*,†,¶] and Liberato Manna[*,†]

[†]Department of Nanochemistry and [§]CompuNet, Istituto Italiano di Tecnologia, via Morego 30, I-16163 Genova, Italy
[‡]Center for Nano Science and Technology@PoliMi, Istituto Italiano di Tecnologia, via Giovanni Pascoli 70/3, I-20133 Milan, Italy
[#]Dipartimento di Chimica e Chimica Industriale, Università degli Studi di Genova, Via Dodecaneso, 31, 16146, Genova, Italy
[⊥]IMEM-CNR, Parco Area delle Scienze 37/A, I-43124 Parma, Italy
[∥]Istituto di Cristallografia, Consiglio Nazionale delle Ricerche, via Amendola 122/O, 70126 Bari, Italy

Supporting Information

ABSTRACT: We report a low-temperature colloidal synthesis of single-layer, five-atom-thick, β-In_2Se_3 nanosheets with lateral sizes tunable from ~300 to ~900 nm, using short aminonitriles (dicyandiamide or cyanamide) as shape controlling agents. The phase and the monolayer nature of the nanosheets were ascertained by analyzing the intensity ratio between two diffraction peaks from two-dimensional slabs of the various phases, determined by diffraction simulations. These findings were further backed-up by comparing and fitting the experimental X-ray diffraction pattern with Debye formula simulated patterns and with side-view high-resolution transmission electron microscopy imaging and simulation. The β-In_2Se_3 nanosheets were found to be indirect band gap semiconductors (E_g = 1.55 eV), and single nanosheet photodetectors demonstrated high photoresponsivity and fast response times.

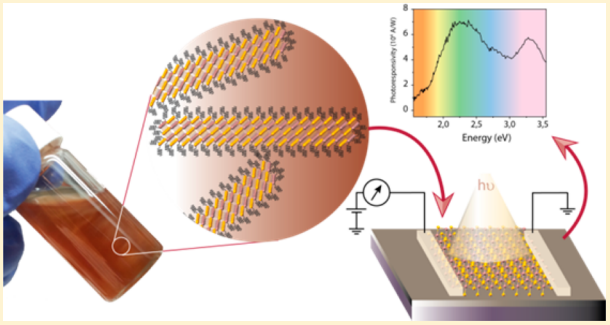

INTRODUCTION

Two-dimensional (2D) semiconductors of layered metal chalcogenides (LMCs) have been widely investigated in order to complement graphene for ultrathin and flexible electronic applications and to assess their potential as replacements for silicon-based electronics.[1] Many 2D LMCs interact strongly with light, leading to high-power-density optoelectronic devices,[2] especially those with post-transition metals (such as In_2Se_3, the focus of this work) which exhibit photoresponsivities higher than their transition metal counterparts.[3] The most popular methods to prepare high-quality 2D LMCs to date have been physical/chemical vacuum deposition and micromechanical cleavage.[4] Unfortunately, the former relies on costly high temperature processes while the latter yields polydisperse samples. In this regard, colloidal chemistry offers a low-temperature route to nanomaterials with unique morphological control and has been proven to be a valid alternative for growing 2D materials for use in solution-processed electronic devices.[5−9] To date, apart from a few works on In_xSe_y nanostructures,[10,11] the colloidal synthesis of layered In_2Se_3 was yet to be demonstrated.

We report here a low-temperature (~200 °C) colloidal synthesis of β-In_2Se_3 nanosheets with monolayer thickness and lateral sizes tunable from ~300 to ~900 nm, using short aminonitriles (dicyandiamide or cyanamide) as shape-controlling agents. The rationale that motivated us to investigate these short-chain aminonitriles as promoters of the growth of nanosheets arises from the observation that a few previous works have exploited short molecules as shape/aggregation controlling agents for growing nanosheets of different materials.[8,12,13] The synthesis of In_2Se_3 nanocrystals, however, requires temperatures at which most commonly used short ligand molecules (for example, short alkylamines or alkylcarboxylic acids) would evaporate. Aminonitriles instead have much higher boiling points, without possessing a long carbon backbone. The monolayer thickness of the as-prepared nanosheets was assessed by a combination of various techniques, above all electron and X-ray diffraction analysis coupled with simulation of the patterns. The experimentally determined optical features of the sheets are supportive of a semiconductor material with an indirect band gap, as also corroborated by calculations reported here. Finally, single sheets, once contacted with Ti/Al or Ti/Au electrodes exhibited fast and remarkably high photoresponsivity across the whole visible spectrum.

Received: October 28, 2016
Published: February 3, 2017

DOI: 10.1021/jacs.6b11255
J. Am. Chem. Soc. 2017, 139, 3005−3011

EXPERIMENTAL SECTION

Materials. Indium(III) chloride ($InCl_3$, 99.999%), indium(III) bromide ($InBr_3$, 99.999%), indium(III) iodide (InI_3, 99.998%), selenourea (98%), dicyandiamide (99%), cyanamide (99%), hexane (95%), toluene (99.8%), 1-octadecene (90%), diethyl ether (99.7%), methanol (99.8%), and *N*,*N*-dimethylformamide (DMF, 99.8%) were purchased from Sigma-Aldrich and used without further purification. Oleylamine (80−90%) was purchased from Acros Organics and filtered through a 0.45 μm PTFE filter before use.

Synthesis of 900 nm In_2Se_3 Nanosheets. All synthesis procedures were undertaken by employing standard Schlenk line techniques assisted by a nitrogen-filled glovebox. $InCl_3$ (10 mg, 45 μmol), oleylamine (1.0 mL), and 1-octadecene (4.0 mL) were loaded into a 25 mL three-neck round-bottomed flask equipped with a thermocouple and a magnetic stirrer and degassed at 100 °C for 1 h. Thereafter the temperature was raised to 215 °C under a dry nitrogen flow, and a solution of selenourea (12 mg, 97 μmol) dissolved in DMF (160 μL) was injected. The initially colorless solution turned yellow then red and then darkened within ca. 5−10 s, indicating the formation of In_xSe_y particles. The mixture was then quickly cooled to below 150 °C with an air-jet and then quickly recovered to 200 °C at which point a solution of dicyandiamide (3.7 mg, 45 μmol) dissolved in DMF (200 μL) was injected to promote the growth of nanosheets. The reaction mixture was allowed to stir for an additional 10 min, and finally the heating mantle was removed to cool the reaction mixture. The final solution was dissolved in 15 mL of toluene and centrifuged at 1500 rpm for 20 min. The nanoparticle-rich supernatant was discarded, and the nanosheet-rich precipitate was redispersed in ca. 5 mL of toluene, hexane, or diethyl ether. Extra centrifugation rounds led to significant aggregation of the nanosheets.

X-ray Diffraction (XRD). Toluene solutions containing the nanosheets were washed twice with methanol (1:1 vol.). The nanosheets were redispersed in diethyl ether and dried to powders under vacuum. The XRD patterns of these powders were then acquired on a Rigaku SmartLab 9 kW diffractometer with the X-ray source operating at 40 kV and 150 mA. The instrument was equipped with a Cu source and a Göbel mirror (to obtain a parallel beam and suppress the Cu Kβ radiation at 1.392 Å) and was used in the $\theta/2\theta$ scan geometry for data acquisition.

Thermogravimetric Analysis (TGA). Analyses were carried out with a TGA Q500-TA instrument. As-synthesized and methanol-washed (same procedure as for XRD) samples were heated from 30 to 600 °C at a heating rate of 5°/min under nitrogen flow (50 mL/min).

Steady-State UV−Vis−NIR Extinction Spectroscopy. Optical extinction spectra of dilute hexane dispersions of nanosheets and nanoparticles were recorded in quartz cuvettes of 1 cm path-length employing a Varian Cary 5000 UV−vis-NIR absorption spectrophotometer. The extinction spectrum of the nanosheet dispersions suffered from a large scattering contribution (see Figures S1f and S3c in the Supporting Information (SI)). To overcome this, the absorption spectrum of the nanosheets was retrieved from their total transmission spectrum recorded on a PerkinElmer Lambda 1050 UV-vis-NIR absorption spectrometer equipped with an integrating sphere. For this measurement the nanosheet dispersion was spin-coated on top of a glass substrate and the reflectance of the sample was accounted for.

Elemental Analysis. All elemental compositions were determined by energy-dispersive X-ray spectroscopy (EDS). Concentrated colloidal solutions were drop-cast onto a Si substrate and measured in a high-resolution scanning electron microscope (SEM) JEOL JSM-7500F equipped with a cold field emission gun, and an Oxford X-Max 80 spectrometer (based on an 80 mm^2 Si drift detector). Standardless quantification was achieved with the Aztec Energy EDS software. Elemental analyses on single nanosheets were performed on a JEOL JEM-2200FS microscope equipped with a Bruker Quantax solid state detector. The composition of the nanosheets was also determined by inductively coupled plasma−optical emission spectroscopy (ICP-OES) analysis performed on aiCAP 6000 spectrometer (Thermo Scientific). The nanosheet solutions were digested in aqua regia overnight and diluted to a known volume prior to the measurements.

Transmission Electron Microscopy (TEM). Bright- and dark-field TEM images and selected area electron diffraction (SAED) patterns were acquired on samples prepared by drop-casting colloidal solutions on carbon-coated 200 mesh copper grids, using a JEOL JEM-1011 microscope (W filament) operated at a 100 kV accelerating voltage. High-resolution TEM (HRTEM) images were acquired on a JEOL JEM-2200FS microscope, operating at 200 kV. The microscope is equipped with a CEOS objective corrector, allowing a resolution below 0.9 Å, and an in-column filter (Ω-type), used to increase the contrast in the images by filtering around the elastically transmitted electrons. To obtain top and side views of the nanosheets, the samples were drop-cast on ultrathin carbon and holey carbon-coated copper grids, respectively.

Electron Energy Loss Spectroscopy (EELS). Quantification of light elements as carbon and nitrogen from the ligands and solvent residuals was performed by using EELS in a FEI G2 transmission microscope equipped with an Enfinium spectrometer (Gatan, Inc.). The spectra were acquired in diffraction mode with a collection semiangle much larger than the convergence semiangle, to ensure higher accuracy quantification.[14]

TEM Simulations. Simulations of HRTEM images and electron diffraction (ED) patterns were performed using the xHREM software (HREM Research, Inc.) in the multislice approximation.[15] For HRTEM, small values of defocus (+25 nm) and spherical aberration (−0.03 mm) were used, as determined from the experimental images, by following the suggestions from Bertoni et al.[16]

XRD Simulations. Atomistic models were used as input structural information to a Debye equation-based simulation program.[17] A crystal lattice made of (200×200×1) unit cells along *a*, *b*, and *c* axes was described in the simulations. The XRD patterns were computed in the angular range of 10°−90° with a 0.04° step, selecting the Kα1−Kα2 Cu doublet as radiation wavelength.

Atomic Force Microscopy (AFM) Topography. The sample was prepared by spin-coating a dilute toluene suspension on a silicon substrate, and the topography measurement was performed with a Park XE-100 instrument.

Raman Spectroscopy. The sample was prepared by drop-casting a concentrated suspension onto a silicon substrate. The measurements were performed with a Renishaw inVia confocal Raman microscope using an excitation wavelength of 514.5 nm with a 50× objective and an incident power of ∼0.4 mW on the samples.

Device Fabrication and Characterization. A dilute dispersion of nanosheets was spin-coated onto a Si substrate coated with 300 nm of thermally grown oxide layer. The substrate was then washed with isopropanol and methanol. The electrodes were patterned with electron beam lithography, and then 4/50 nm Ti/Au layers were thermally evaporated. The devices were measured with a probe station in a vacuum chamber. Time-dependent photoresponse measurements were performed using a mechanical chopper to modulate the incident laser beam. The output current was allowed to pass through a preamplifier before being recorded with an oscilloscope. Here we define the rise (fall) time as the time elapsed between 10% (90%) and 90% (10%) of I_{max}. Detectivities were calculated considering the shot noise from the dark current as the main source of noise.

Density Functional Theory (DFT) Calculations. DFT-D2[18] calculations were performed using the Perdew−Burke−Enzerhof functional, Martin−Trouillers norm-conserving pseudo potentials for all elements, and the pwscf code.[19] Values of 100 and 400 Ryd were used as cutoffs for the plane waves and charge density, respectively. A uniform 6×6×3 mesh was used for Brillouin zone sampling of a bulk model, obtained by expanding one layer over *c* to yield a multilayered crystal with AA stacking. The optimized lattice parameters of the hexagonal unit cell were a = 3.96 Å and c/a = 2.36, consistent with previous calculations on In_2Se_3 crystals.[20] From the bulk model a monolayer with stacking Se-In-Se-In-Se was extracted. Periodic slab calculations with a vacuum gap of 15 Å were performed using a Monkhorst−Pack 6×6×1 k-point mesh. The frequency-dependent dielectric function was computed using the random-phase approx-

DOI: 10.1021/jacs.6b11255
J. Am. Chem. Soc. 2017, 139, 3005−3011

imation, by employing the epsilon.x tool of pwscf. The static limit of the dielectric function was computed using uniform 6×6×1, 12×12×1, and 16×16×1 meshes, obtaining values of respectively 4.08, 3.83, and 3.78, as an indicator of the simulation convergence. We finally used the 16×16×1 mesh for calculation using an interband smearing factor of 0.3 eV. The absorption coefficient was computed as an average of the two dielectric tensor diagonal components, which are perpendicular to the light propagation direction. Additionally, a rigid upshift of 0.7 eV has been applied to the conduction bands, in order to match the onset of the absorption profile with that of the experimental data. Results have then been compared with GW data. GW stands for the product of the Green's function G and the screened electron−electron interaction W.

RESULTS AND DISCUSSION

The sheets were grown in two steps (Figure 1): First, indium selenide nanocrystals were formed by reacting $InCl_3$ and selenourea at 215 °C in the presence of oleylamine (Figure 1a). The particles had average size of 5 nm and average composition of $In_{1.8}Se_3$. Next, at 200 °C, a second injection containing a stoichiometric amount of dicyandiamide (in DMF) with respect to indium enabled the formation, within a few minutes, of hexagonally shaped nanosheets (Figure 1b) with $In_{2.1}Se_3$ composition, that is, close to In_2Se_3.

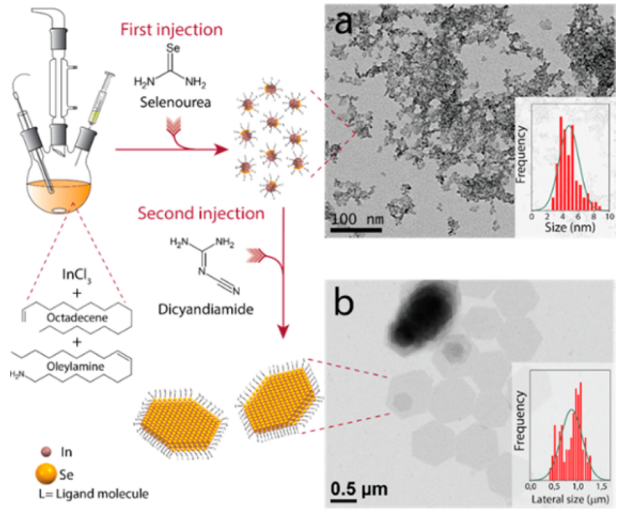

Figure 1. Schematic showing the growth of In_2Se_3 nanosheets by a two-step process. Representative TEM images of (a) $In_{1.8}Se_3$ nanocrystals formed upon injection of selenourea and (b) In_2Se_3 nanosheets formed subsequently upon injection of a short amino-nitrile.

Control experiments in which the second injection consisted of just DMF (i.e., without the dicyandiamide) yielded only 5 nm indium selenide particles with a composition of $In_3Se_{1.92}$ along with larger Se particles (see Figures S1a,b in the SI), proving an active key role of dicyandiamide in the 2D growth. Sheets could also be grown by using cyanamide instead of dicyandiamide (Figure S1c). A clarification on whether these ligands promote oriented attachment or templated growth by selectively passivating the basal facets of In_2Se_3 will, however, require further studies. Most likely the sheets grow separately and feed on these initially formed nuclei and unreacted precursors. Partial support to this hypothesis comes from the fact that we failed to observe intermediate products in which partially formed sheets exhibited irregular shapes (i.e., different from hexagonal). Shape control was lost when $InCl_3$ was replaced with other indium halides (Figure S2). This was probably due to the increase in the size of the halide ion upon moving from Cl^- to Br^- to I^-, which reduces the Lewis acidic nature of the indium precursor and renders them less prone toward accepting a lone pair of electrons from the amino-nitriles, making them less reactive in the process. However, a more systematic investigation is needed to unravel the growth mechanism, which will constitute our future work.

The average lateral dimensions of the In_2Se_3 nanosheets could be tuned by varying the concentration of oleylamine. For instance, by increasing its volume fraction from 20% to 60%, the lateral size could be tuned from 900 to 300 nm (Figure S3a). The simultaneous injection of selenourea and dicyandiamide at 200 and 215 °C could equally deliver small nanocrystals at the early stages of the reaction, followed by the formation of sheets (Figure S4). However, in this case, the sheets were heavily stacked. Stacking was also observed for the sheets prepared by the two-injection approach, albeit to a lower extent. The tendency to form stacks was accentuated by addition of polar solvents and by centrifugation.

Discerning between the many possible phases with In_2Se_3 composition is difficult since this system exhibits an intricate polymorphism,[20−30] especially in the few-layers range, as also

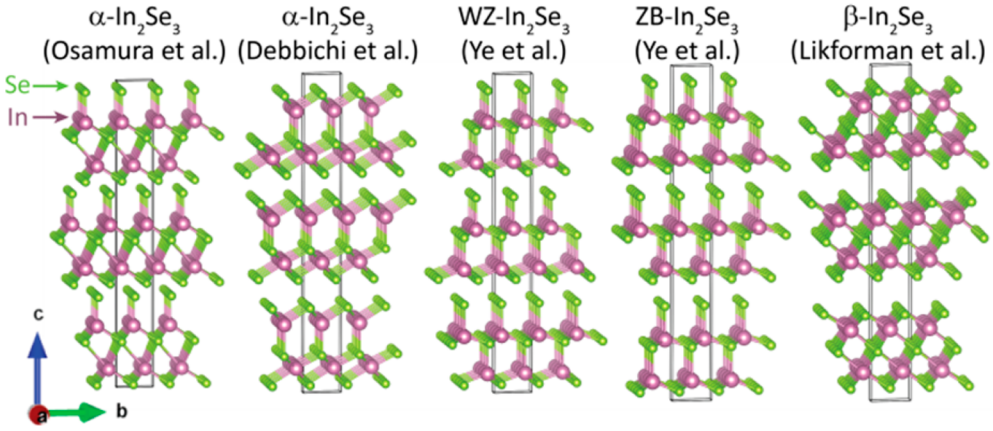

Figure 2. Structural models for the various proposed layered structures of In_2Se_3 (Se atoms depicted in green, In in purple) with van der Waals gap between adjacent Se planes. From left to right: α-In_2Se_3 (Osamura et al.);[22] α-In_2Se_3 (Debbichi et al.);[20] WZ-In_2Se_3 (Ye et al.);[29] ZB-In_2Se_3 (Ye et al.);[29] and β-In_2Se_3 (Likforman et al.).[24]

DOI: 10.1021/jacs.6b11255
J. Am. Chem. Soc. 2017, 139, 3005−3011

demonstrated by Zhou et al.[31] In In_2Se_3, one-third of the cationic sites are vacant.[21] Either these vacancies order in a screw arrangement along the *c*-axis, giving rise to the enantiomorphous γ-In_2Se_3,[32] or they cluster on one close-packed plane along the [001] direction, giving rise to the layered phases (which crystallize in either the $R3m$ or $R\bar{3}m$ space group).[20,22,26,27,29] The literature concerning stable phases, phase transitions, and properties of In_2Se_3 is not always consistent.[20−23,25,27−30] It is commonly held that, in ambient conditions, only two layered phases exist, usually denoted as α and β, both semiconducting, with respective band gaps of 1.35 and 1.45 eV and with very different electrical conductivities: in bulk, the α phase is more conductive by 2 orders of magnitude than the β phase.[30,31,33−37] In reality, the crystal structures of the α and β phases have never been completely confirmed (in particular that of the α phase), and several models have been proposed to describe them, as sketched in Figure 2. Both phases consist of covalently bonded 5-atom-thick monolayers stacked in an ABC sequence, and they all share a very similar *a*-parameter (4.00−4.05 Å). Thus, the α and β structures, for either a monolayer or a few-layer flake, become indistinguishable from a simple qualitative analysis of their diffraction patterns. The structures mainly differ in the coordination geometry of the indium atoms, which can be tetrahedral, octahedral, or mixed. Moreover, due to the peculiar ABC stacking, the {100} reflection is symmetry forbidden for all the structures in the bulk.[29]

Here, in order to distinguish the crystal structure and the number of layers in the In_2Se_3 sheets that we have synthesized, we combined HRTEM and XRD with ED from [001] oriented nanosheets. The latter method has previously been used to determine the thickness of graphene flakes.[38] ED simulations were performed to calculate the intensity ratio between {100} and {110} reflections ($R = I_{\{100\}}/I_{\{110\}}$) as a function of the number of layers for all the proposed structures. The results are plotted in Figure 3a and show that one-layer and two-layer flakes of most structures can be distinguishable within the experimental error. A typical ED from a single nanosheet is presented in Figure 3b demonstrating its single-crystal quality.

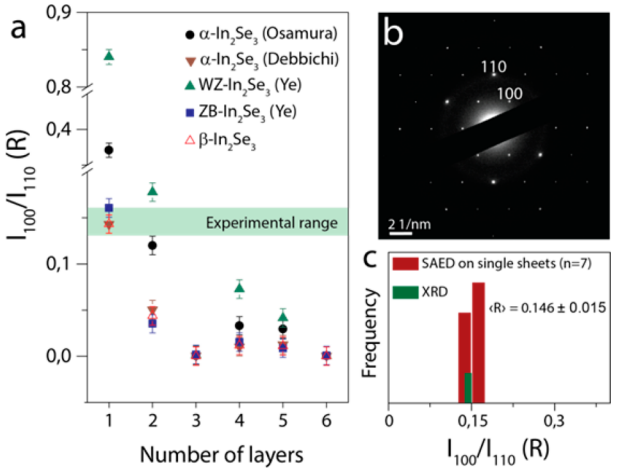

Figure 3. (a) ED simulations from [001] oriented nanosheets: integrated intensity ratio between (100) and (110) peaks as a function of the number of layers for all the structural models considered in Figure 2. (b) Typical SAED pattern of a single In_2Se_3 nanosheet. (c) Distribution of intensity ratios obtained experimentally from several SAED patterns on single nanosheets and from the XRD pattern.

The {100} reflection is well visible, indicating its ultrathin nature. An experimental average intensity ratio of $R = 0.146 \pm 0.015$ was found from several ED patterns as plotted in Figure 3c. The {100} reflection could also be observed in the XRD (Figure 4a) from a nanosheet powder, and a similar intensity

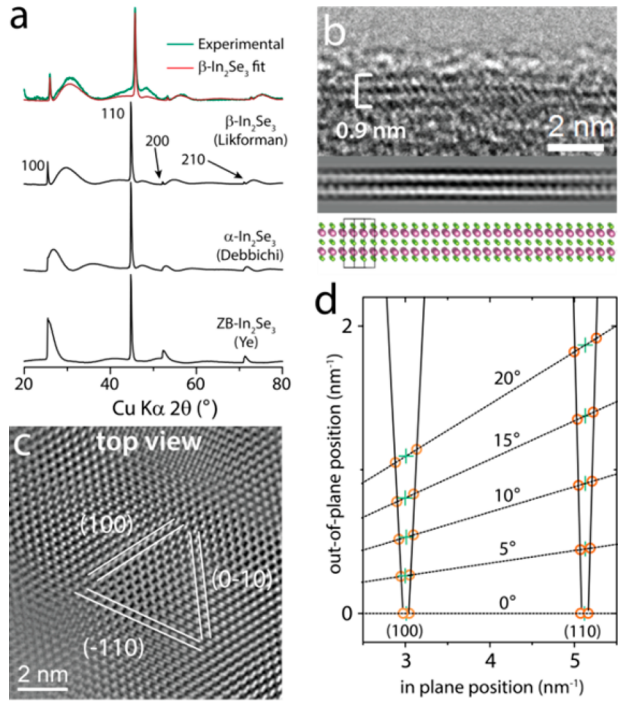

Figure 4. (a) Experimental XRD pattern (in green) of In_2Se_3 nanosheet powder and simulated patterns for 2D single layers from β (Likforman),[24] α (Debbichi),[20] and ZB (Ye)[29] structures. A Debye refinement of the β structure was performed and the fit (in red) is shown along with the experimental pattern (green). (b) HRTEM side-view image of a folded nanosheet on a holey TEM grid along with a simulated image 1° away from the [210] axis, and the corresponding view of the structure model, to reproduce the small tilt in the experimental image. (c) HRTEM top-view image, and (d) broadening of the {100} and {110} diffraction spots upon tilting.

ratio was found ($R = 0.14 \pm 0.02$). This *R* value is in agreement with predicted values for some of the structures with monolayer thickness. The monolayer nature could be seen by HRTEM of side-views of folded sheets. An example is shown in Figure 4b: the contrast in the experimental image (top panel) is in good agreement with the one obtained from a simulation of a single layer (middle panel). Due to the experimental conditions of imaging, the white fringes correspond to the In planes (see the sketch at the bottom of Figure 4b). From the simulation of ED patterns and from the HRTEM side view, we can conclude that the nanosheets consist of single layers of In_2Se_3. Moreover, two of the proposed structures, i.e., α-In_2Se_3 from Osamura et al.[22] and the WZ-In_2Se_3 from Ye et al.,[29] can be excluded due to their high *R* values. However, three structures give very similar results: the α-In_2Se_3 and β-In_2Se_3 structures as proposed by Debbichi et al.[20] and Likforman et al.,[24] and the ZB-In_2Se_3 one from Ye et al.[29] All these three structures give $R = 0.14 \pm 0.01$, and consequently a very similar contrast in HRTEM in top-view [001] orientation (Figure 4c).

A conclusive determination of the structure from side-view HRTEM alone was not possible, due to contrast change depending on defocus, even if a good match with simulations

DOI: 10.1021/jacs.6b11255
J. Am. Chem. Soc. 2017, 139, 3005−3011

was found for β-In_2Se_3 (as shown in the middle panel of Figure 4b). We therefore simulated the XRD patterns for monolayer 2D slabs of the three structures that gave similar R values from ED simulations and compared them to the experimental pattern (see Figure 4a). The best match was given by the β-In_2Se_3 proposed by Likforman et al.[24] A small contraction of the a-parameter was found (a_{exp} = 3.97 Å, −0.85%). The fit (red pattern in Figure 4a) is in good agreement with the experimental pattern (in green, Figure 4a). In addition, we have also simulated the XRD patterns for thicker 2D slabs of β-In_2Se_3 (Figure S5). As expected, as the number of layers increases, the broad peaks become narrower, and additional peaks appear. Thus, we suggest that XRD, *per se*, can be a useful tool to determine the number of layers.

The presence of the ligands on the surface of the sheets (even after extensive washing) was confirmed by elemental and thermogravimetric analysis, as detailed in the SI (see Figures S6 and S7). The passivation of the sheets explains their average thickness of 3 nm, as determined by atomic force microscopy measurements (Figures S8 and S9a).[8] We therefore concluded that these hexagonal nanosheets are organic-passivated, single-crystal 6-Å-thick monolayers of β-In_2Se_3 with a slightly contracted a-parameter (−0.85%) compared to the bulk. The same conclusions could be drawn for the smaller 300 nm nanosheets (Figures S3b and S9b). Similarly to other 2D crystals, the surface of these 5-atom-thick monolayers exhibits rippling, as demonstrated by the broadening of the diffraction spots upon tilting (Figure 4d).[39,40] The presence of ripples changes the cylindrical shape of the rods that constitute the reciprocal lattice of a perfect 2D crystal into cones.[39] Consequently, the diffraction spots broaden upon tilting. The amplitude of the ripples can be inferred from the angle of the cone. In the present case their amplitude was below 1 nm.

Raman spectroscopy is a powerful technique for structural investigation,[41] especially for 2D materials where the position of the shear and layer breathing modes can be exploited for the reliable determination of the number of layers, and the absence of these is characteristic of the monolayer nature.[42−45] Unfortunately, these peaks are typically located in the ultralow-frequency region, which is difficult to study experimentally. Bulk β-In_2Se_3 is known to exhibit three Raman peaks in the 100−210 cm^{-1} region corresponding to the A^1_{1g} (110 cm^{-1}), E^2_g (180 cm^{-1}), and A^2_{1g} (205 cm^{-1}) modes. The E^2_g peak is weak and fades away in the few layer regime.[30,33,46] The Raman spectrum of as-synthesized β-In_2Se_3 nanosheets synthesized by us is reported in Figure S10. We observed a peak at ca. 205 cm^{-1} which can be attributed to the A^2_{1g} mode of β-In_2Se_3. Another peak at ca. 250 cm^{-1} was found to evolve with increasing exposure time, and it can be attributed to amorphous selenium.[47] Ultrathin In_2Se_3 layers had been previously reported to be easily damaged during Raman measurements.[30] Indeed, upon vacuum annealing the nanosheets we observed that at temperatures above 200 °C a fraction of the chalcogen atoms was lost (Figure S11). This observation is in line with other recent studies which have shown that thin flakes of layered chalcogenides of post-transition metals are metastable.[30,48,49]

We also recorded the absorption spectrum of the as-synthesized β-In_2Se_3 nanosheets (Figure 5, black curve). This was done using a spectrometer equipped with an integrating sphere, which assisted in accounting for the reflectance of the sample while extracting the absorption spectrum from the recorded transmission spectrum, thereby removing the scattering contribution that plagued the solution extinction spectrum (Figures S1f and S3c). The absorption spectrum is characterized by a slow rise in absorption around the absorption edge (i.e., lack of a clear absorption onset), typical of indirect semiconductors. A value of 1.55 eV for the band gap was extracted by a Tauc plot analysis (Figure 5 inset).

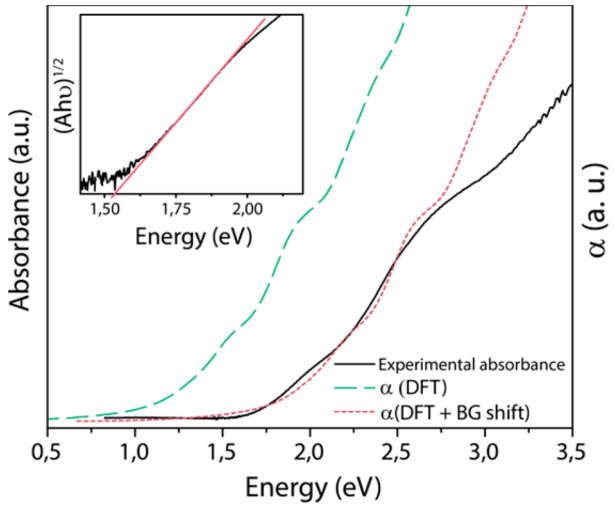

Figure 5. Experimental absorption spectrum (black curve) of β-In_2Se_3 nanosheets along with the calculated absorption spectrum for a single β-In_2Se_3 monolayer (green and red curves). An optical band gap of 1.55 eV was determined by a Tauc plot analysis, as shown in the inset.

Bulk β-In_2Se_3 has a direct band gap of 1.3 eV.[35] Our data indicate that at the monolayer limit the c-axis quantum confinement translates into an increase of the band gap to 1.5 eV (this small increase can be explained by the poor electronic coupling between layers in layered materials). Also, a direct to indirect band gap transition is likely to occur as the crystal becomes thinner, similar to the reverse transition in semiconducting transition metal dichalcogenides.[50,51] Indeed, Balakrishnan et al.[33] have observed quenching of the photoluminescence in few layers β-In_2Se_3 when reducing the number of layers. In line with this observation, at the monolayer limit we observed no photoluminescence from our nanosheets. We have additionally computed the electronic band-structure for monolayer β-In_2Se_3 (Figure S12a), which confirms its indirect band gap, with the lowest energy transition connecting the Γ and M symmetry points. The computed absorption coefficient (Figure 5, green curve) matches the experimental absorption spectrum only after applying a 0.7 eV upward shift to the DFT conduction band levels (Figure 5, red curve). Our results show that plain DFT grossly underestimates the band gap of the materials. At the GW level the band gap appears in better agreement with experiments but is still underestimated, the reported value being 1.29 eV.[20]

Single β-In_2Se_3 monolayers were then contacted with Ti/Al or Ti/Au electrodes as shown in Figure 6a (inset). The dark current was below our detection limit of 0.5 pA within the applied voltage range for all samples, which is most likely due to the high contact resistance formed by a reversed biased Schottky barrier. Typical current−voltage curves under illumination with laser light in the visible for Ti/Au electrodes are displayed in Figure 6a. They demonstrate an almost linear behavior. For Ti/Al electrodes the current was nonlinear with increasing bias voltage (Figure S13a), demonstrating a low current plateau around zero bias and then a superlinear increase

DOI: 10.1021/jacs.6b11255
J. Am. Chem. Soc. 2017, 139, 3005−3011

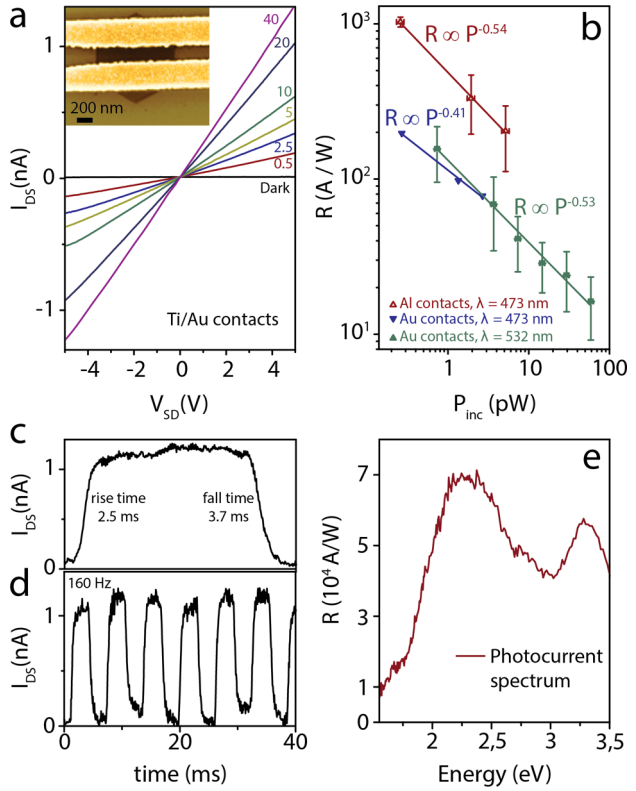

Figure 6. (a) Current−voltage curves recorded from a single monolayer β-In_2Se_3 nanosheet contacted with Ti/Au electrodes in the dark and upon illumination with a 532 nm laser, at different intensities (denoted in mW/cm^2). The inset shows a SEM image of a single β-In_2Se_3 nanosheet contacted by two metal electrodes. (b) Photocurrent responsivity of six different single β-In_2Se_3 nanosheet devices. (c,d) Time response of the current of a single β-In_2Se_3 nanosheet device when the laser beam is switched on and off (c), and modulated by a mechanical chopper at 160 Hz (d). (e) Photocurrent spectrum of a β-In_2Se_3 monolayer nanosheet device under illumination of a xenon lamp coupled to a monochromator, recorded at a bias voltage of 10 V (lower panel). The impinging light power is in the fW range, which leads to responsivity values up to 7×10^4 A/W.

for bias voltages larger than ±1 V. Overall, devices with Ti/Al contacts manifested higher current at high bias as compared to Ti/Au electrodes. This might be related to the lower work function of Al (around 4 eV) compared to Au (around 5 eV) that results in a smaller Schottky barrier at the reverse biased contact. The responsivity, $R = I_{ph}/P_{inc}$, where P_{inc} is the incident light power on the sheet area between the contacts and $I_{ph} = I_{light} - I_{dark}$, is shown versus incident laser power in Figure 6b for six different devices. The behavior can be well described by an inverse power-law[33,37,52] with responsivities in the 10^3 A/W range at low laser power (few pW) for the devices with Ti/Al electrodes. Other figures of merit, such as external quantum efficiency and detectivity, are shown in Figure S13b,c.

The time-dependent photoresponse is shown in Figure 6c, with a rise time of 2.5 ms and a fall time of 3.7 ms. Consequently, modulation frequencies of up to 160 Hz could be well resolved (Figure 6d). These values of photoresponsivity and response times are comparable to the best photodetectors based on single- and few-layer 2D semiconductors that were reported so far,[3] and in particular to those of multilayer β-In_2Se_3, which implies a higher photoresponsivity per layer in the monolayer regime.[33] Finally, the spectral dependence of the photocurrent of a single β-In_2Se_3 nanosheet device is shown in Figure 6e, where a broad band centered at 2.3 eV, a pronounced low-energy shoulder at around 1.6 eV, and a narrower high-energy band at 3.3 eV can be identified. We note that the photocurrent spectra were recorded from single sheets on which metal layers for electrical contacts were deposited, while the absorption spectrum was taken from a film of nanosheets. This can account for the differences between photocurrent and absorption spectra.

CONCLUSIONS

We have developed a colloidal synthesis of β-In_2Se_3 monolayer sheets with lateral size-control up to the micrometer range. The crystal structure and the number of layers were determined by diffraction methods. In principle, the intensity ratio method used here to determine the number of layers can be extended to other layered materials crystallizing in the same space group such as Bi_2Se_3, Sn_2Te_3, and others. The as-synthesized β-In_2Se_3 sheets exhibited fast and remarkably high photoresponse over the full visible range. This makes them very appealing for device applications in layered structures with other 2D materials, for example by deposition onto graphene as ultrasensitive photodetectors. Future directions will include unravelling the role of aminonitriles in the shape control of nanocrystals of materials that, like In_2Se_3, require high temperatures for their 2D growth.

ASSOCIATED CONTENT

Supporting Information

The Supporting Information is available free of charge on the ACS Publications website at DOI: 10.1021/jacs.6b11255.

Control experiments and additional structural, optical, and electrical characterizations; nanosheet surface characterization using elemental and thermogravimetric analyses; AFM topographic measurements; Raman spectroscopy and study of thermal stability of the nanosheets; calculated electronic band structure and density of states of β-In_2Se_3 (PDF)

AUTHOR INFORMATION

Corresponding Authors

*sandeep.ghosh@iit.it; sandeep.ghosh@utexas.edu
*liberato.manna@iit.it

ORCID

Giovanni Bertoni: 0000-0001-6424-9102
Roman Krahne: 0000-0003-0066-7019
Liberato Manna: 0000-0003-4386-7985

Present Address

¶McKetta Department of Chemical Engineering, The University of Texas at Austin, Austin, Texas 78712-1589, United States.

Notes

The authors declare no competing financial interest.

ACKNOWLEDGMENTS

The authors gratefully acknowledge F. Bonaccorso and A. E. Del Rio Castillo for stimulating discussions and for help with the Raman measurements. The research leading to these results has received funding from the FP7 under grant agreement no. 614897 (ERC Consolidator Grant "TRANS-NANO") and from Horizon 2020 research and innovation programme

DOI: 10.1021/jacs.6b11255
J. Am. Chem. Soc. 2017, 139, 3005−3011

H2020-Adhoc-2014-20 under grant agreement no. 696656 – GrapheneCore1.

REFERENCES

(1) Wang, Q. H.; Kalantar-Zadeh, K.; Kis, A.; Coleman, J. N.; Strano, M. S. *Nat. Nanotechnol.* **2012**, *7*, 699−712.
(2) Eda, G.; Maier, S. A. *ACS Nano* **2013**, *7*, 5660−5665.
(3) Buscema, M.; Island, J. O.; Groenendijk, D. J.; Blanter, S. I.; Steele, G. A.; van der Zant, H. S.; Castellanos-Gomez, A. *Chem. Soc. Rev.* **2015**, *44*, 3691−3718.
(4) Butler, S. Z.; Hollen, S. M.; Cao, L.; Cui, Y.; Gupta, J. A.; Gutiérrez, H. R.; Heinz, T. F.; Hong, S. S.; Huang, J.; Ismach, A. F.; Johnston-Halperin, E.; Kuno, M.; Plashnitsa, V. V.; Robinson, R. D.; Ruoff, R. S.; Salahuddin, S.; Shan, J.; Shi, L.; Spencer, M. G.; Terrones, M.; Windl, W.; Goldberger, J. E. *ACS Nano* **2013**, *7*, 2898−2926.
(5) Nasilowski, M.; Mahler, B.; Lhuillier, E.; Ithurria, S.; Dubertret, B. *Chem. Rev.* **2016**, *116*, 10934−10982.
(6) Yoo, D.; Kim, M.; Jeong, S.; Han, J.; Cheon, J. *J. Am. Chem. Soc.* **2014**, *136*, 14670−14673.
(7) Vaughn, D. D.; In, S.-I.; Schaak, R. E. *ACS Nano* **2011**, *5*, 8852−8860.
(8) Schliehe, C.; Juarez, B. H.; Pelletier, M.; Jander, S.; Greshnykh, D.; Nagel, M.; Meyer, A.; Foerster, S.; Kornowski, A.; Klinke, C.; Weller, H. *Science* **2010**, *329*, 550−553.
(9) Dogan, S.; Bielewicz, T.; Cai, Y.; Klinke, C. *Appl. Phys. Lett.* **2012**, *101*, 073102.
(10) Park, K. H.; Jang, K.; Kim, S.; Kim, H. J.; Son, S. U. *J. Am. Chem. Soc.* **2006**, *128*, 14780−14781.
(11) Lauth, J.; Gorris, F. E. S.; Khoshkhoo, M. S.; Chasse, T.; Friedrich, W.; Lebedeva, V.; Meyer, A.; Klinke, C.; Kornowski, A.; Scheele, M.; Weller, H. *Chem. Mater.* **2016**, *28*, 1728−1736.
(12) Ithurria, S.; Dubertret, B. *J. Am. Chem. Soc.* **2008**, *130*, 16504−16505.
(13) Shamsi, J.; Dang, Z.; Bianchini, P.; Canale, C.; Stasio, F. D.; Brescia, R.; Prato, M.; Manna, L. *J. Am. Chem. Soc.* **2016**, *138*, 7240−7243.
(14) Bertoni, G.; Verbeeck, J. *Ultramicroscopy* **2008**, *108*, 782−790.
(15) Kirkland, E. J. *Advanced Computing in Electron Microscopy*, 2nd ed.; Springer: New York, 2010.
(16) Bertoni, G.; Grillo, V.; Brescia, R.; Ke, X.; Bals, S.; Catellani, A.; Li, H.; Manna, L. *ACS Nano* **2012**, *6*, 6453−6461.
(17) Debye, P. *Ann. Phys.* **1915**, *351*, 809−823.
(18) Grimme, S.; Antony, J.; Ehrlich, S.; Krieg, H. *J. Chem. Phys.* **2010**, *132*, 154104.
(19) Giannozzi, P.; Baroni, S.; Bonini, N.; Calandra, M.; Car, R.; Cavazzoni, C.; Ceresoli, D.; Chiarotti, G. L.; Cococcioni, M.; Dabo, I.; Dal Corso, A.; de Gironcoli, S.; Fabris, S.; Fratesi, G.; Gebauer, R.; Gerstmann, U.; Gougoussis, C.; Kokalj, A.; Lazzeri, M.; Martin-Samos, L.; Marzari, N.; Mauri, F.; Mazzarello, R.; Paolini, S.; Pasquarello, A.; Paulatto, L.; Sbraccia, C.; Scandolo, S.; Sclauzero, G.; Seitsonen, A. P.; Smogunov, A.; Umari, P.; Wentzcovitch, R. M. *J. Phys.: Condens. Matter* **2009**, *21*, 395502.
(20) Debbichi, L.; Eriksson, O.; Lebegue, S. *J. Phys. Chem. Lett.* **2015**, *6*, 3098−3103.
(21) Newman, P. C. *J. Phys. Chem. Solids* **1962**, *23*, 19−23.
(22) Osamura, K.; Murakami, Y.; Tomiie, Y. *J. Phys. Soc. Jpn.* **1966**, *21*, 1848−1848.
(23) Popović, S.; Čelustka, B.; Bidjin, D. *Phys. Status Solidi A* **1971**, *6*, 301−304.
(24) Likforman, A.; Guittard, M. *Compt. Rend.* **1974**, *279*, 33−35.
(25) van Landuyt, J.; van Tendeloo, G.; Amelinckx, S. *Phys. Status Solidi A* **1975**, *30*, 299−314.
(26) Popović, S.; Tonejc, A.; Gržeta-Plenković, B.; Čelustka, B.; Trojko, R. *J. Appl. Crystallogr.* **1979**, *12*, 416−420.
(27) Likforman, A.; Fourcroy, P.-H.; Guittard, M.; Flahaut, J.; Poirier, R.; Szydlo, N. *J. Solid State Chem.* **1980**, *33*, 91−97.
(28) Lutz, H. D.; Fischer, M.; Baldus, H. P.; Blachnik, R. *J. Less-Common Met.* **1988**, *143*, 83−92.
(29) Ye, J.; Soeda, S.; Nakamura, Y.; Nittono, O. *Jpn. J. Appl. Phys.* **1998**, *37*, 4264.
(30) Tao, X.; Gu, Y. *Nano Lett.* **2013**, *13*, 3501−3505.
(31) Zhou, J.; Zeng, Q.; Lv, D.; Sun, L.; Niu, L.; Fu, W.; Liu, F.; Shen, Z.; Jin, C.; Liu, Z. *Nano Lett.* **2015**, *15*, 6400−6405.
(32) Pfitzner, A.; Lutz, H. D. *J. Solid State Chem.* **1996**, *124*, 305−308.
(33) Balakrishnan, N.; Staddon, C. R.; Smith, E. F.; Stec, J.; Gay, D.; Mudd, G. W.; Makarovsky, O.; Kudrynskyi, Z. R.; Kovalyuk, Z. D.; Eaves, L.; Patanè, A.; Beton, P. H. *2D Mater.* **2016**, *3*, 025030.
(34) Bidjin, D.; Popović, S.; Čelustka, B. *Phys. Status Solidi A* **1971**, *6*, 295−299.
(35) Julien, C.; Chevy, A.; Siapkas, D. *Phys. Status Solidi A* **1990**, *118*, 553−559.
(36) Jacobs-Gedrim, R. B.; Shanmugam, M.; Jain, N.; Durcan, C. A.; Murphy, M. T.; Murray, T. M.; Matyi, R. J.; Moore, R. L.; Yu, B. *ACS Nano* **2014**, *8*, 514−521.
(37) Island, J. O.; Blanter, S. I.; Buscema, M.; van der Zant, H. S. J.; Castellanos-Gomez, A. *Nano Lett.* **2015**, *15*, 7853−7858.
(38) Meyer, J. C.; Geim, A. K.; Katsnelson, M. I.; Novoselov, K. S.; Obergfell, D.; Roth, S.; Girit, C.; Zettl, A. *Solid State Commun.* **2007**, *143*, 101−109.
(39) Meyer, J. C.; Geim, A. K.; Katsnelson, M. I.; Novoselov, K. S.; Booth, T. J.; Roth, S. *Nature* **2007**, *446*, 60−63.
(40) Brivio, J.; Alexander, D. T. L.; Kis, A. *Nano Lett.* **2011**, *11*, 5148−5153.
(41) Bonaccorso, F.; Tan, P.-H.; Ferrari, A. C. *ACS Nano* **2013**, *7*, 1838−1844.
(42) Tan, P. H.; Han, W. P.; Zhao, W. J.; Wu, Z. H.; Chang, K.; Wang, H.; Wang, Y. F.; Bonini, N.; Marzari, N.; Pugno, N.; Savini, G.; Lombardo, A.; Ferrari, A. C. *Nat. Mater.* **2012**, *11*, 294−300.
(43) Lui, C. H.; Ye, Z.; Keiser, C.; Xiao, X.; He, R. *Nano Lett.* **2014**, *14*, 4615−4621.
(44) Zhang, X.; Qiao, X.-F.; Shi, W.; Wu, J.-B.; Jiang, D.-S.; Tan, P.-H. *Chem. Soc. Rev.* **2015**, *44*, 2757−2785.
(45) Zhao, Y.; Luo, X.; Zhang, J.; Wu, J.; Bai, X.; Wang, M.; Jia, J.; Peng, H.; Liu, Z.; Quek, S. Y.; Xiong, Q. *Phys. Rev. B: Condens. Matter Mater. Phys.* **2014**, *90*, 245428.
(46) Zhou, S.; Tao, X.; Gu, Y. *J. Phys. Chem. C* **2016**, *120*, 4753−4758.
(47) Lucovsky, G.; Mooradian, A.; Taylor, W.; Wright, G. B.; Keezer, R. C. *Solid State Commun.* **1967**, *5*, 113−117.
(48) Buha, J.; Gaspari, R.; Del Rio Castillo, A. E.; Bonaccorso, F.; Manna, L. *Nano Lett.* **2016**, *16*, 4217−4223.
(49) Sutter, E.; Huang, Y.; Komsa, H. P.; Ghorbani-Asl, M.; Krasheninnikov, A. V.; Sutter, P. *Nano Lett.* **2016**, *16*, 4410−4416.
(50) Mak, K. F.; Lee, C.; Hone, J.; Shan, J.; Heinz, T. F. *Phys. Rev. Lett.* **2010**, *105*, 136805.
(51) Splendiani, A.; Sun, L.; Zhang, Y.; Li, T.; Kim, J.; Chim, C.-Y.; Galli, G.; Wang, F. *Nano Lett.* **2010**, *10*, 1271−1275.
(52) Tamalampudi, S. R.; Lu, Y.-Y.; Kumar U, R.; Sankar, R.; Liao, C.-D.; Moorthy B, B. K.; Cheng, C.-H.; Chou, F. C.; Chen, Y.-T. *Nano Lett.* **2014**, *14*, 2800−2806.

DOI: 10.1021/jacs.6b11255
J. Am. Chem. Soc. 2017, 139, 3005−3011